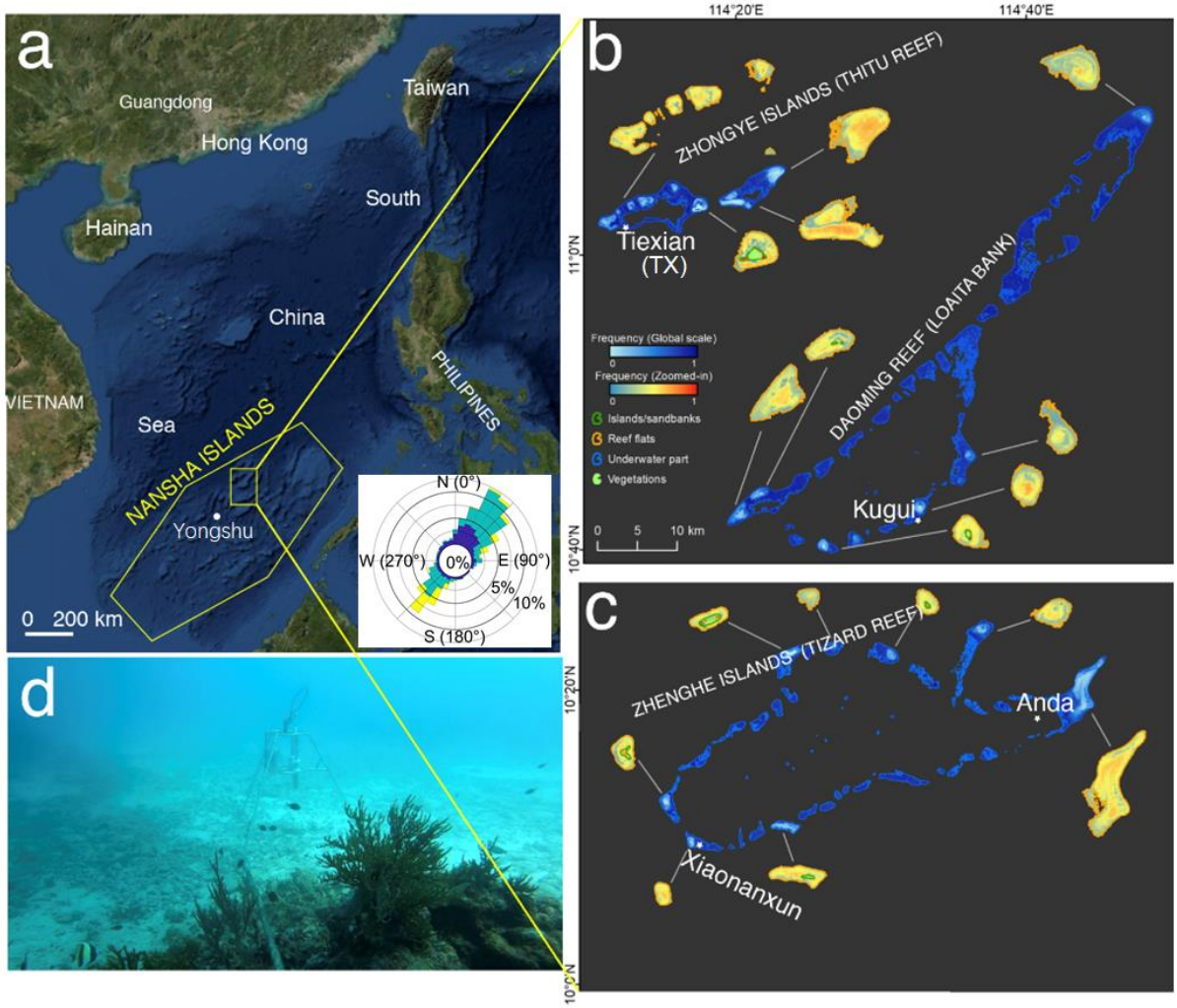

Figure 1 The study area: (a) Satellite image (from the website earthexplorer.usgs) of atolls and submerged reef banks comprising the Nansha Islands, South China Sea; the wind rose is based on the annual CFSv2 wind speed data from 2018; (b) and (c) the site at Tiexian Reef for *in situ* tripod mooring observations for 8 months at the 12-m deep reef flat, adjusted with permission from [*Dong et al.*, 2019]; and (d) an underwater photo from the observation site at Tiexian Reef. The other three sites for tidal-cycle observations in the Kugui, Anda, and Xiaonanxun Reefs (located in the Zhongye, Daoming and Zhenghe Islands, respectively). Figures 1b and 1c show reef flats shallower than 20 and the inundation frequency of coral reef islands (motu); shallow reef flats and islands are denoted and zoomed in with yellow to red colors, where fully inundated reef flats are blue [*Dong et al.*, 2019].

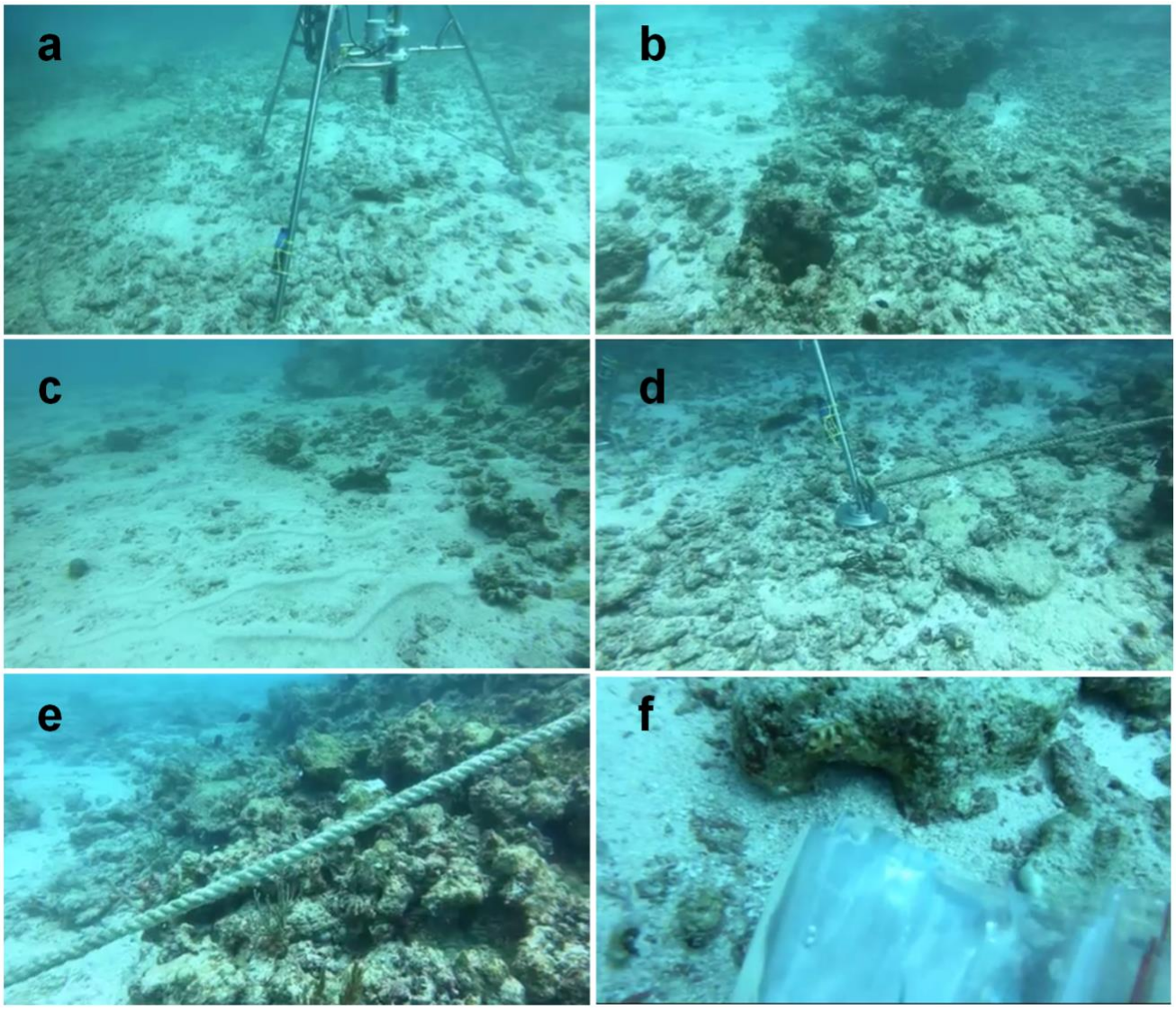

Figure 2 Underwater photographs of the deep flat at Tiexian (TX) Reef: (a) the location of hydrodynamic observation of the sandy bed; (b, c, d, e) ripples are widely developed even during the relatively low-energy season (March-April), interspersed with coral rubble and branches; and (f) sediment sample collection near the mooring tripod.

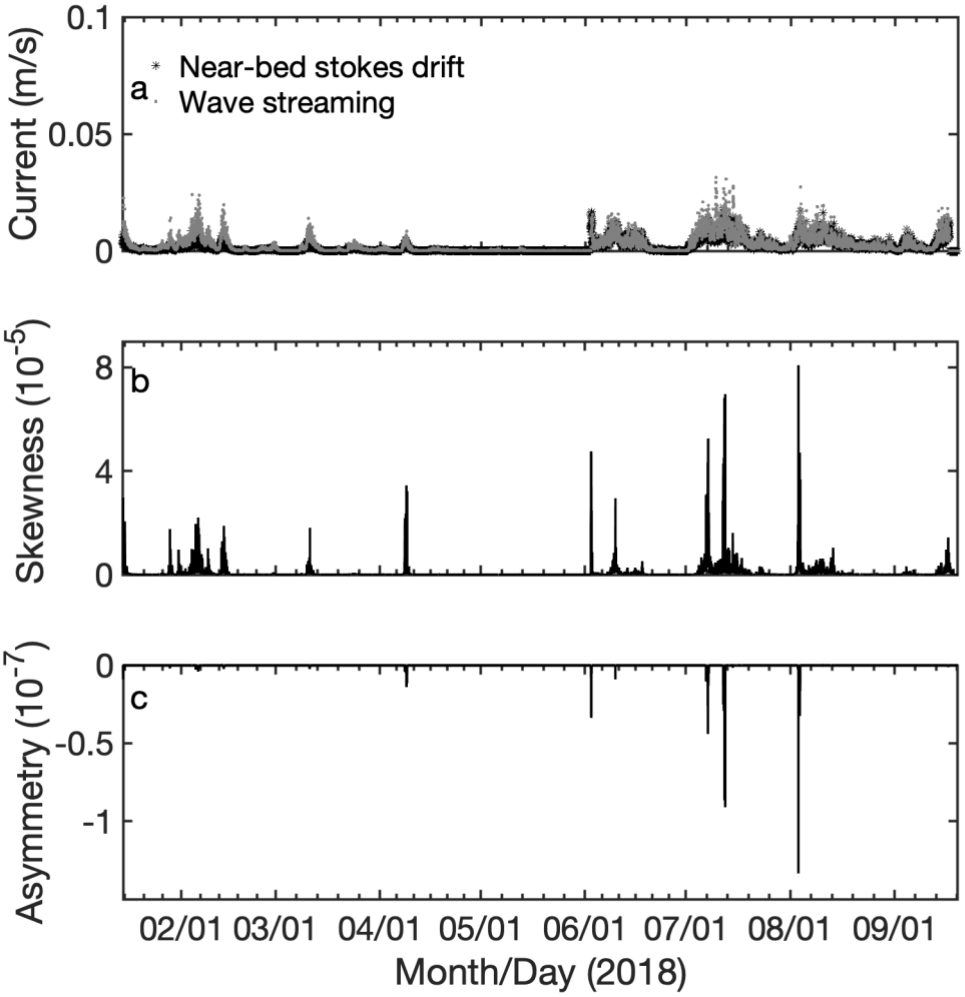

Figure 3 Wave parameters: (a) wave-induced current speed, (b) wave skewness, and (c) asymmetry.

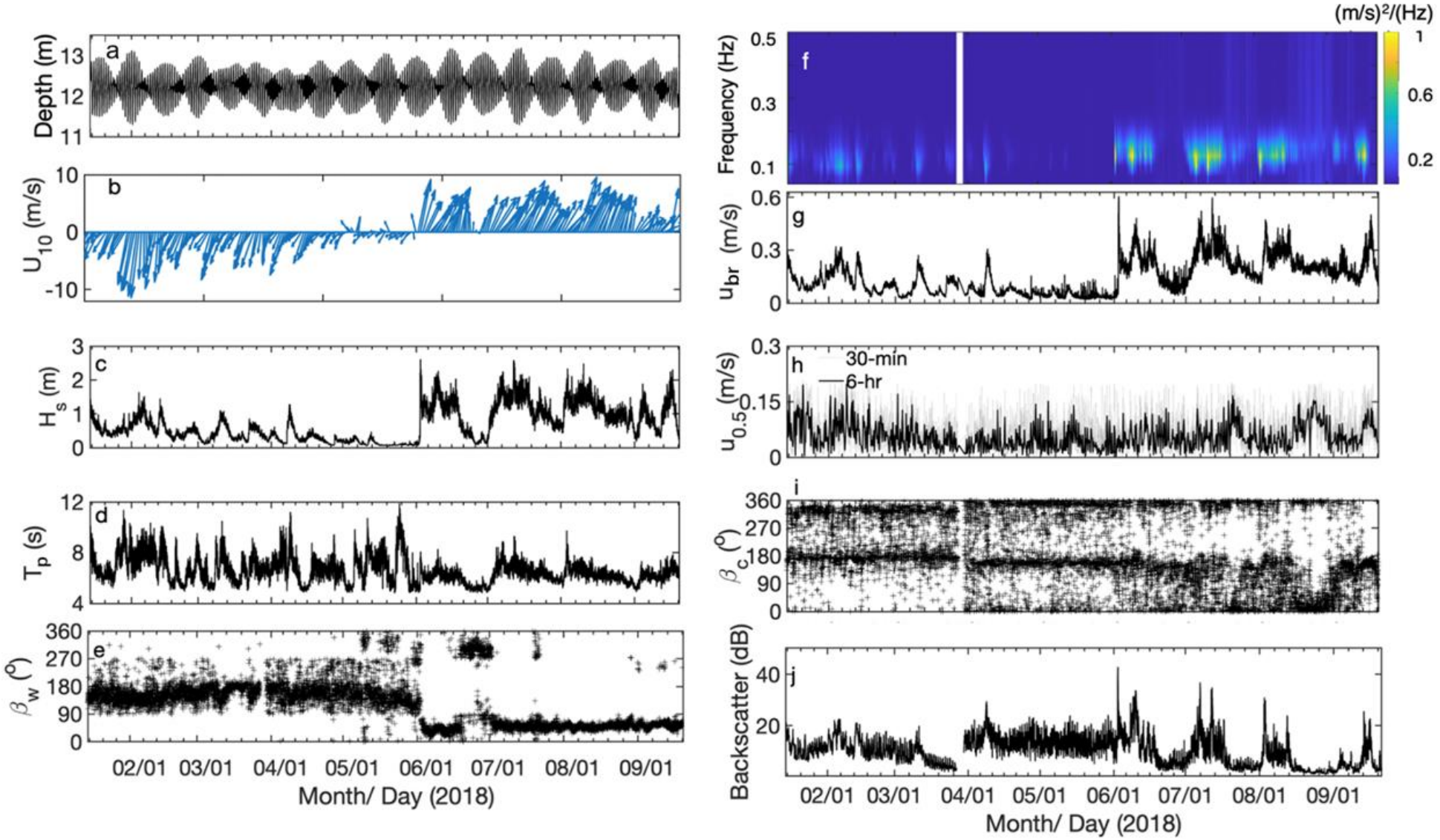
a
Depth (m)
13
12
11
b
U_{10} (m/s)
10
0
-10
c
H_s (m)
3
2
1
0
d
T_p (s)
12
8
4
e
β_w (°)
360
270
180
90
0
02/01 03/01 04/01 05/01 06/01 07/01 08/01 09/01
Month/ Day (2018)
(m/s)²/(Hz)
f
Frequency (Hz)
0.5
0.3
0.1
1
0.6
0.2
g
u_{br} (m/s)
0.6
0.3
0
h
30-min
6-hr
$u_{0.5}$ (m/s)
0.3
0.15
0
i
β_c (°)
360
270
180
90
0
j
Backscatter (dB)
40
20
02/01 03/01 04/01 05/01 06/01 07/01 08/01 09/01
Month/ Day (2018)

Figure 4 Hydrodynamic conditions during the *in situ* observation at Tiexian (TX) Reef: (a) water level changes; (b) wind velocity at 10 m above the sea surface from NCEP Climate Forecast System Version 2 (CFSv2) (arrows represent the direction the wind blowing towards); (c) significant wave height H_s; (d) peak wave period T_p and (e) wave propagation direction β_w derived from ADV measurements in azimuth degrees, i.e., in a numerical measure that moves around the wind rose in a clockwise circle from 0 degrees (N) to 360 degrees (N); (f) combined horizontal velocity spectrum; (g) representative bottom orbital velocity u_{br} based on 16Hz current velocity; (h) mean current velocity at 0.5 m above seabed; (i) current direction; and (j) acoustic backscatter recorded by ADV located at 0.5 m above the seabed.

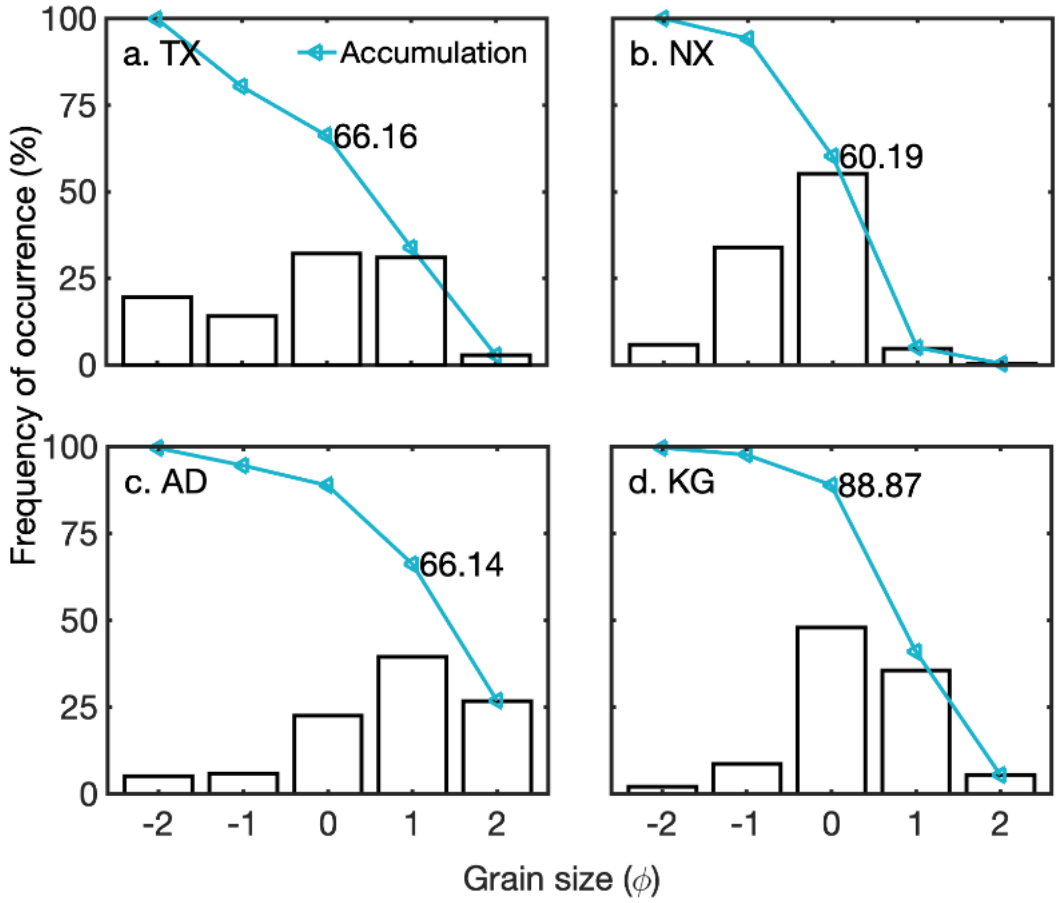

Figure 5 Grain size distribution of reef sediment samples collected from (a) Tiexian (d_{35}=0.5 mm, d_{50} =1 mm, d_{90} =4 mm), (b) Xiaonanxun (d_{50} =1 mm, d_{90} = 2 mm), (c) Anda (d_{50} =0.5 mm, d_{90} =2 mm), and (d) Kugui Reef (d_{50} =1 mm, d_{90} = 2 mm).

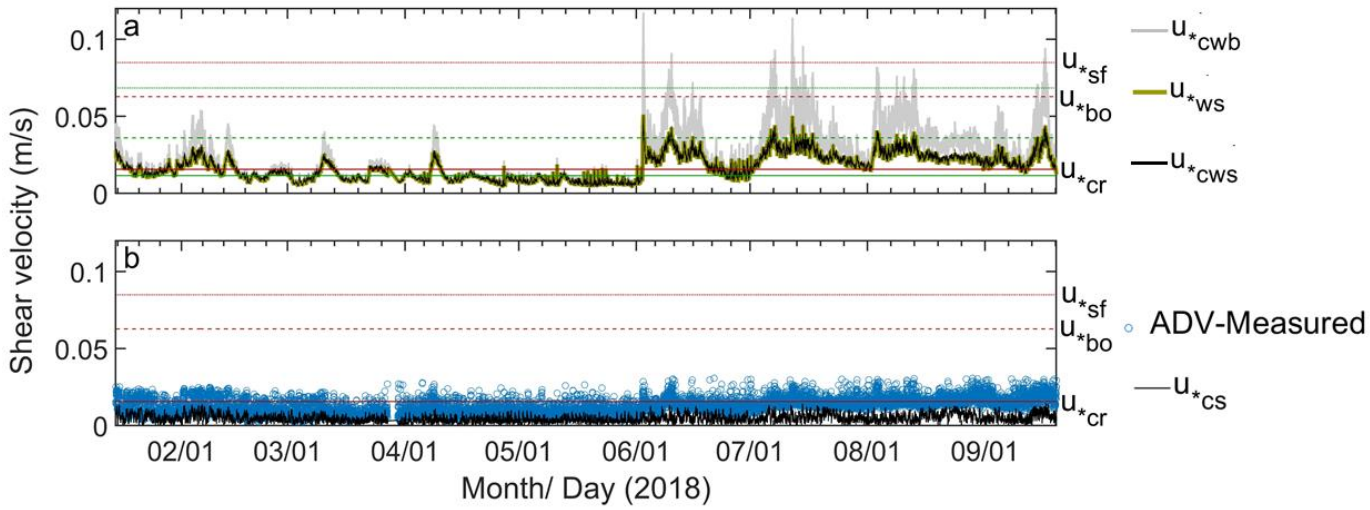

Figure 6 Skin-friction related shear velocities due to (a) waves (u_{*ws}) and combined wave-current interactions (u_{*cws}), and associated with bedload transport (u_{*cwb}); and (b) current only (u_{*cs}), and measured Reynolds shear velocity with ADV. Critical shear velocities for transport (bedload) initiation u_{*cr}, ripple breakoff (suspended load initiation) u_{*bo}, and sheet flow (ripple removal) u_{*sf} for median grain size d_{50} = 1 mm and d_{35} = 0.5 mm are represented by red and green solid, dashed and dotted lines, respectively.

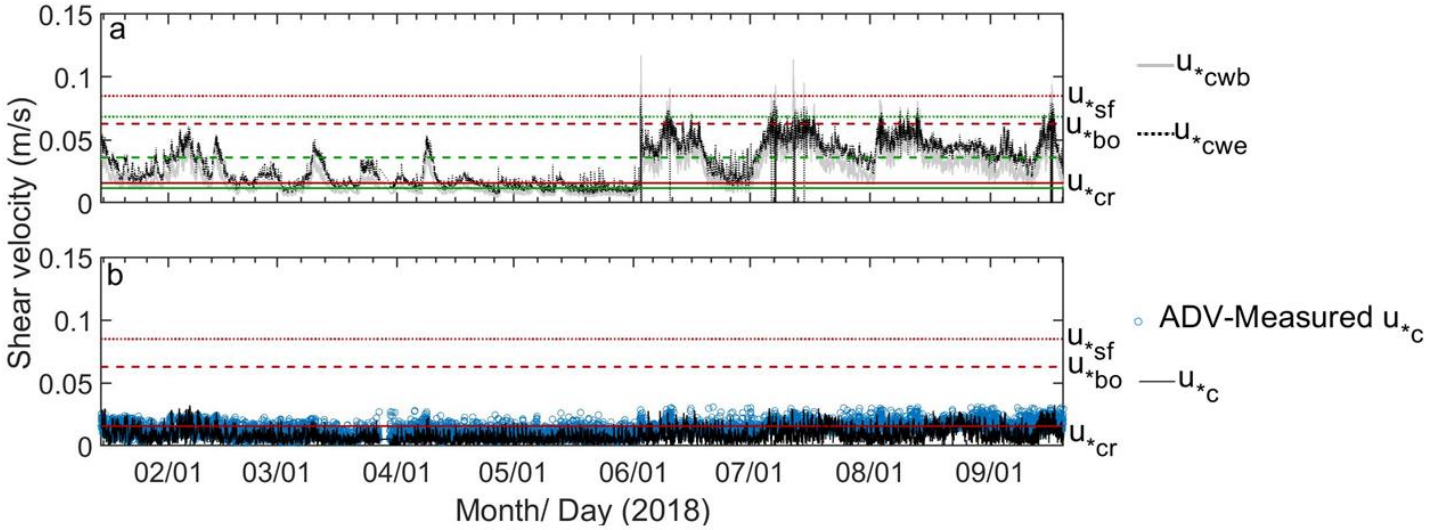

Figure 7 (a) Enhanced combined wave-current shear velocity associated with preceding ripples (u_{*cwe}) and bedload transport (u_{*cwb}), as calculated with preceding ripple geometry and roughness height k_{bs}+k_{bb}, respectively. (b) Current-only shear velocity associated with total physical roughness (u_{*c}). Here u_{*c} appears more approximate to the mean shear velocity measurement by ADV, as calculated with GM86 model and the total physical roughness height $k_b = k_{bs}+k_{bb}+k_{br}$. Critical shear velocities for bedload transport u_{*cr}, ripple breakoff u_{*bo}, and sheet flow u_{*sf} for median grain size d_{50} = 1 mm and d_{35} = 0.5 mm are represented by red and green solid, dashed and dotted lines, respectively.

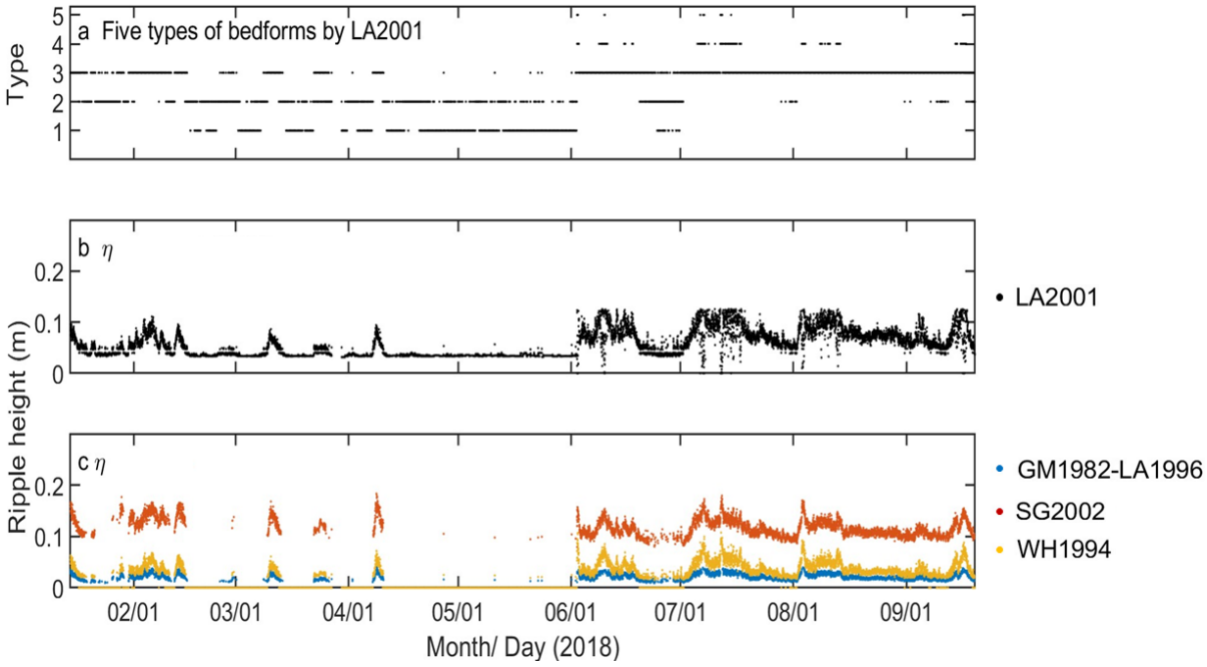

Figure 8 Predicted ripple geometries: (a) Five types of bedforms calculated by using Li and Amos 2001 model (LA2001); (b) ripple height estimated using the Li and Amos 2001 model (LA2001). (c) Estimation of ripple heights using the Grant and Madsen 1982 (GM1982-LA1996), Styles and Glenn 2002 (SG2002), and Wiberg and Harris 1994 (WH1994) models, respectively.

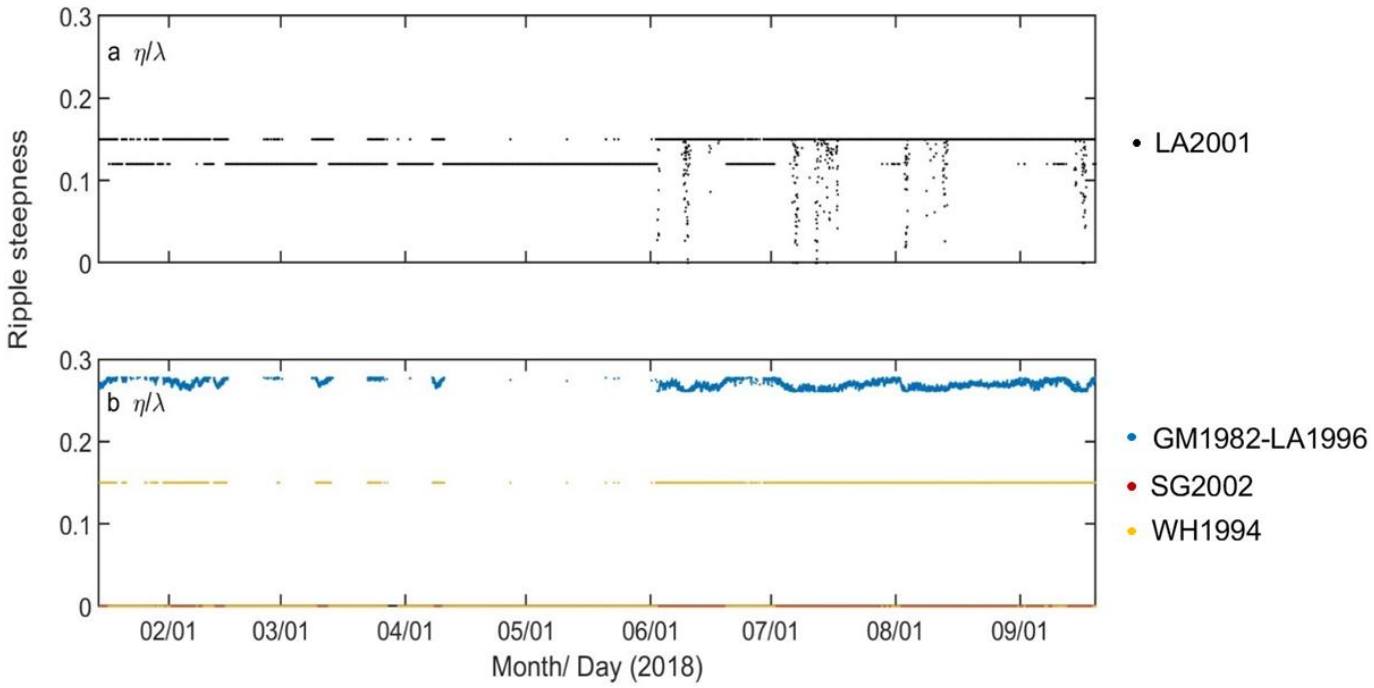

Figure 9 Predicted steepness of four ripple predictors: (a) Li and Amos, 2001 (LA2001); and (b) Grant and Madsen 1982 (GM1982-LA1996); Styles and Glenn, 2002 (SG2002); Wiberg and Harris, 1994 (WH1994).

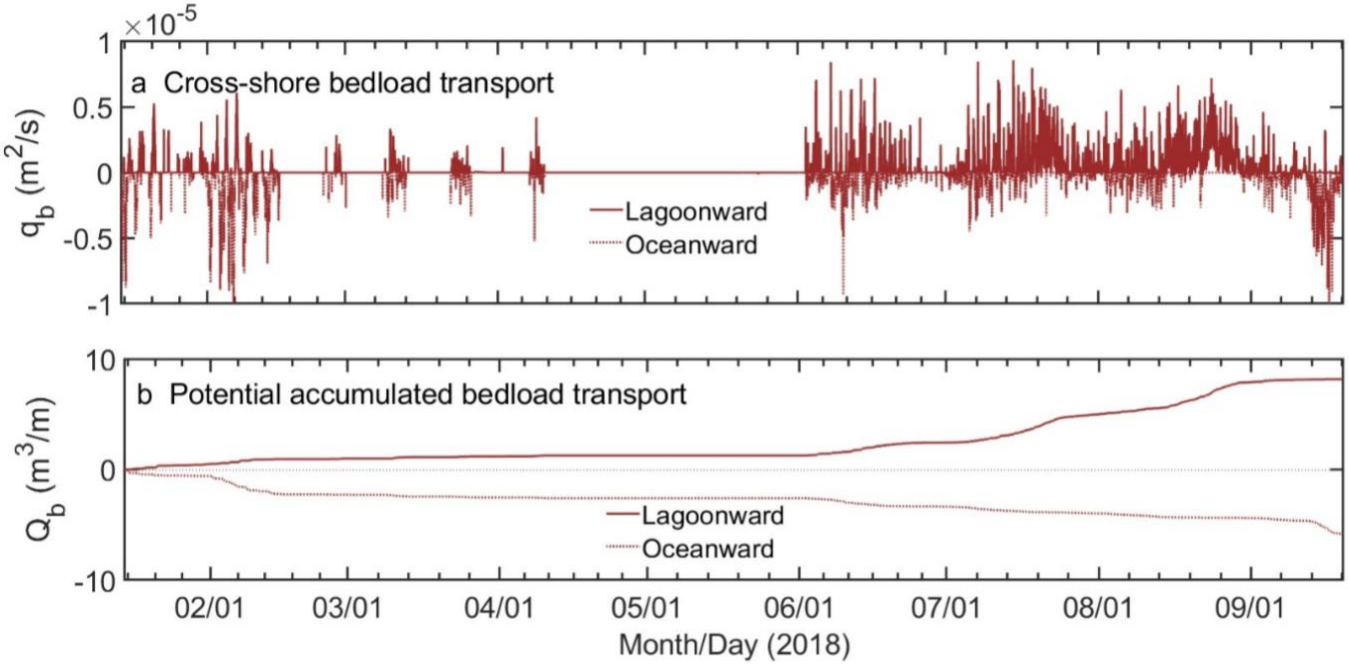

Figure 10 Potential bedload transport calculations: (a) cross-shore bedload transport under symmetric waves plus current, as a function of skin-friction wave-current combined shear stresses and current shear stresses; and (b) accumulated transport during the 8-month observation. Because sediment availability is limited in reef environment, bedload transport computations only provide an upper limit of the "potential" sediment transport .

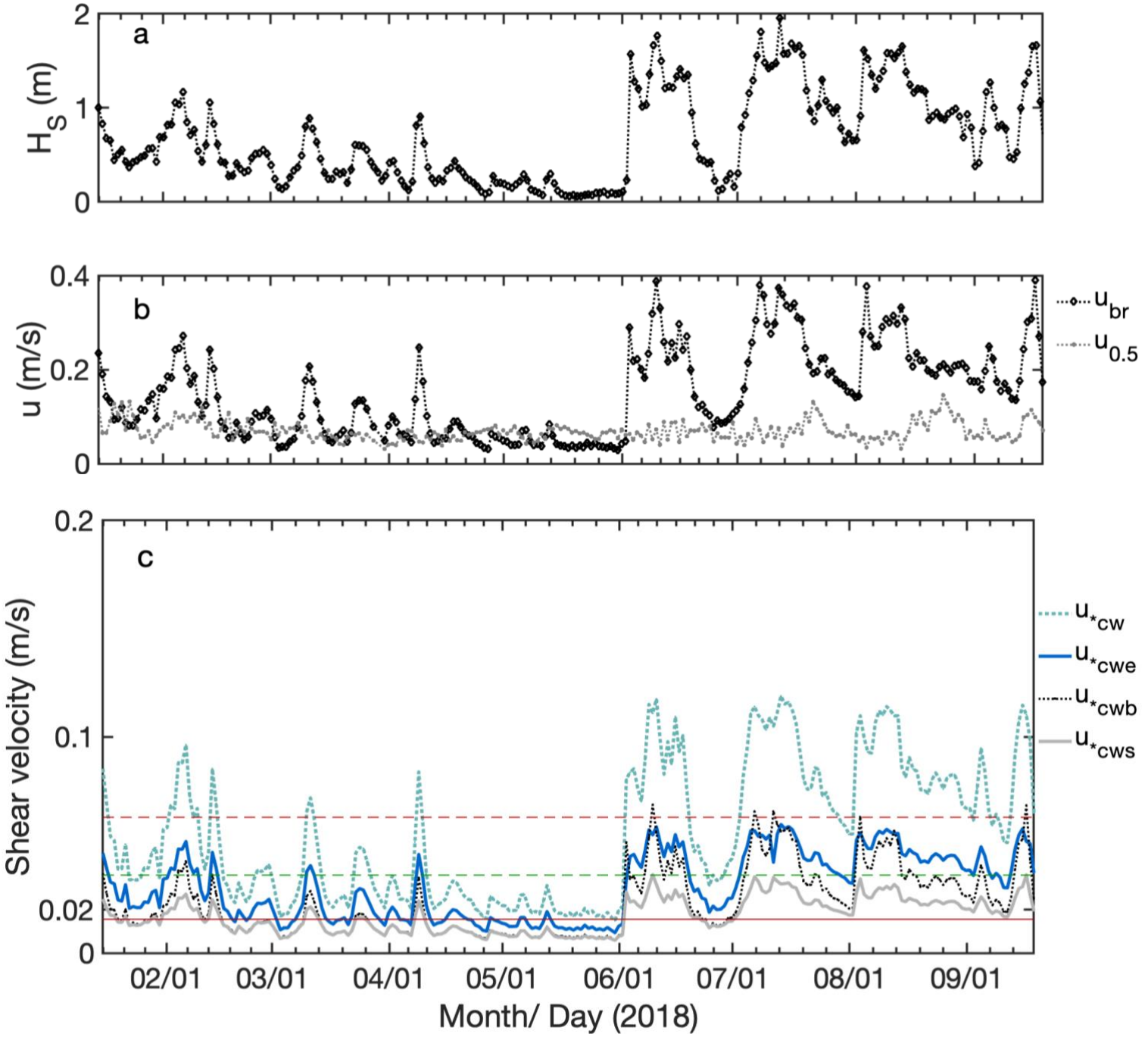

Figure 11 (a) The 1-day average of the observed significant wave height H_s, (b) representative bottom orbital velocity u_{br}, mean current velocity $u_{0.5}$, and (c) shear velocities. The total shear velocity could be smaller than the theoretical total shear velocity u_{*cw} that was calculated from the total roughness height ($k_b = k_{bs}+k_{bt}+k_{br}$) due to limited bed sediment. Critical shear velocities for transport (bedload) u_{*cr}, ripple breakoff u_{*bo}, and sheet flow (ripple removal) u_{*sf} for median grain size d_{50} = 1 mm are represented by red solid, dashed and dotted lines respectively. Critical shear velocities for ripple break-off (suspended transport initiation) u_{*bo} for d_{35} = 0.5 mm was also marked as green dashed line.